

COHERENT INTERFEROMETRY IN FINELY LAYERED RANDOM MEDIA*

LILIANA BORCEA[†], GEORGE PAPANICOLAOU[‡], AND CHRYSOULA TSOGKA[§]

Abstract. We study broadband, coherent interferometric array imaging (CINT) in finely layered media in a regime with strong fluctuations. By coherent interferometric imaging we mean the backpropagation of time-windowed cross correlations of the array data. For waves propagating over long distances, there is statistical stabilization of the traces observed at the array. They have the form of a coherent signal that can be described by the O’Doherty–Anstey (ODA) theory, followed by long and noisy codas. We show that coherent interferometry exploits the time coherence in the data, leading to stable images. Moreover, we prove that in this regime only the ODA behavior plays a role in the imaging, and we quantify explicitly the resolution of CINT in terms of this time coherence and the array aperture. We illustrate the theory with numerical simulations.

Key words. O’Doherty–Anstey theory, imaging, layered media

AMS subject classifications. 35B40, 35F10, 82D30, 45Q05, 65R32

DOI. 10.1137/050633524

1. Introduction. Broadband array imaging in cluttered environments arises in important applications such as ultrasonic imaging and nondestructive testing, ground or foliage penetrating radar, shallow water sonar, seismic exploration, etc. The typical imaging setup consists of small or distributed sources or scatterers buried in clutter and a remote array \mathcal{A} of N transducers at which we record the traces of the received signal

$$(1.1) \quad P(\vec{\mathbf{x}}_r, t), \quad \vec{\mathbf{x}}_r \in \mathcal{A}, \quad t \in (t_1, t_2), \quad r = 1, \dots, N,$$

for a time window (t_1, t_2) . When imaging sources, the excitation comes from them, usually in the form of a short pulse

$$(1.2) \quad f(t) = e^{-i\omega_0 t} f_B(t),$$

with carrier frequency ω_o and bandwidth B . In this case the array is passive, meaning it has only receivers. Imaging of scatterers requires active arrays, where pulses such as (1.2) are sent from some transducers in \mathcal{A} and the traces (1.1) are the recorded echoes.

For brevity, we focus our attention on the simplest array imaging problem of a point source at unknown location $\vec{\mathbf{y}}$, emitting the pulse (1.1) at $t = 0$. Our goal is not only the estimation of $\vec{\mathbf{y}}$ from the traces (1.1), which can be done with very

*Received by the editors June 13, 2005; accepted for publication (in revised form) November 4, 2005; published electronically February 15, 2006.

<http://www.siam.org/journals/mms/5-1/63352.html>

[†]Computational and Applied Mathematics, MS 134, Rice University, 6100 Main Street, Houston, TX 77005-1892 (borcea@caam.rice.edu). This author’s research was supported in part by NSF grants DMS-0305056 and DMS-0354658 and by grant ONR N00014-05-1-0699.

[‡]Department of Mathematics, Stanford University, Stanford, CA 94305 (papanico@math.stanford.edu). This author’s research was supported by grants ONR N00014-02-1-0088 and 02-SC-ARO-1067-MOD 1.

[§]Department of Mathematics, University of Chicago, Chicago, IL 60637 (tsogka@math.uchicago.edu). This author’s research was supported by grants ONR N00014-02-1-0088 and 02-SC-ARO-1067-MOD 1.

few measurements. Instead, we use the whole array and view the result as the point spread function of the imaging method that we propose. Then extensions to the more general problem of imaging distributed sources or scatterers follow easily.

In this paper we consider only acoustic waves and not elastic ones, as is more appropriate for geophysical applications. The acoustic model can be used for imaging when mostly pressure waves propagate and shear waves can be neglected. Even though this acoustic model does not account for mode conversion, it is often used in geophysical applications as well. We analyze here imaging in finely layered media in a regime with strong fluctuations that we assume to be unknown.

Imaging in smooth and known media is done efficiently with Kirchhoff migration and its numerous variants used in seismic imaging [17, 7, 6], radar [19, 11, 15], etc. These methods are based on high frequency asymptotic techniques, and they seek to estimate the source at \vec{y} by migrating traces (1.1) to a search location \vec{y}^s using the travel time $\tau(\vec{x}_r, \vec{y}^s)$ between the transducer at \vec{x}_r and \vec{y}^s . The Kirchhoff migration imaging functional is

$$(1.3) \quad \mathcal{I}^{\text{KM}}(\vec{y}^s) = \sum_{r=1}^N P(\vec{x}_r, \tau(\vec{x}_r, \vec{y}^s)),$$

and it peaks at \vec{y} because of the approximate cancellation of phases in the summation over the array on the right side of (1.3). In the ideal situation of an infinite bandwidth B and aperture a of the array, the Kirchhoff migration point spread function is $\mathcal{I}^{\text{KM}}(\vec{y}^s) \sim \delta(\vec{y} - \vec{y}^s)$ and the estimation of the source is perfect in smooth and known media. In practice, this ideal resolution is never achieved because of limited bandwidth and aperture, so our image will be blurred. In a remote sensing regime, where the array aperture is much smaller than the range η of the source, the range and cross-range resolution limits have a simple expression if the medium is uniform with speed of propagation c_o . Then the range uncertainty is $O\left(\frac{\pi c_o}{B}\right)$ and the array aperture affects only the cross-range resolution, which is given by $O\left(\frac{\pi c_o \eta}{Ba}\right)$ (see, for example, [7]). We discuss Kirchhoff migration in more detail in section 2.3 and explain there how it becomes unstable (statistically) in cluttered media, in regimes with significant multipathing of the waves by the clutter, where traces (1.1) have long and noisy codas.

It is pointed out in [10, 9, 14] that to stabilize the imaging process in cluttered media we should first cross-correlate traces (1.1) over appropriate space-time windows, in order to create the so-called coherent interferograms. We then migrate them to \vec{y}^s by means of the deterministic travel times $\tau(\vec{x}_r, \vec{y}^s)$. This approach is called coherent interferometry, and it is studied theoretically and numerically in [10, 9] for isotropic clutter. In this paper we consider the case of finely layered media with strong fluctuations, as encountered in geophysical problems where well log measurements near the surface of the earth reveal velocity profiles as in Figure 1. For simplicity, we consider fluctuations about a uniform propagation velocity c_o , but extensions to general smooth, three-dimensional average velocity profiles are possible.

The main result of the paper is that coherent interferometry works in essentially the same way as in isotropic clutter, which may be surprising considering the very different wave scattering regimes considered here and in [10]. The isotropic clutter in [10] is weak, so most scattering is in the forward direction, whereas here we take the other extreme of layered clutter, where there is very strong backscattering of the waves by the layers. The fact that coherent interferometry works in basically the same way in these two extreme cases indicates its potentially wide applicability.

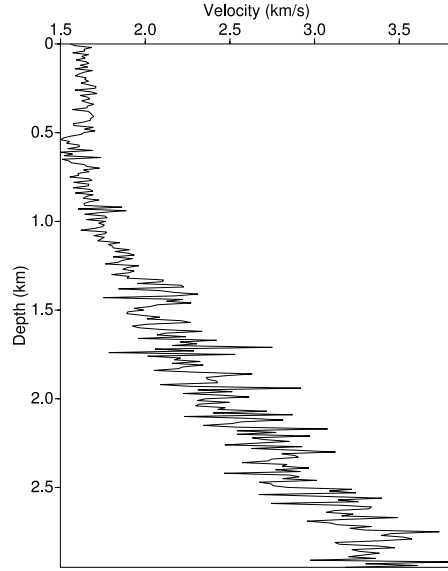


FIG. 1. *Example of a simulated pressure wave velocity profile in the earth.*

In isotropic media there are two key, clutter dependent parameters that determine in a definitive way the quality of our image: the decoherence length X_d and frequency Ω_d . If we have good estimates of these parameters, then we can form stable images in clutter, with resolution limits $O\left(\frac{\pi c_o}{\Omega_d}\right)$ and $O\left(\frac{\pi c_o \eta}{B X_d}\right)$ in range and cross-range, respectively [10]. These resolution estimates look very similar to those for Kirchhoff migration in the absence of clutter, except for two important differences: the bandwidth in the range resolution is replaced by Ω_d and the aperture in the cross-range resolution is replaced by X_d . Usually, $\Omega_d \ll B$ and $X_d \ll a$, so the images in clutter are blurrier than in homogeneous backgrounds, as expected. However, the images are stable, with explicitly quantified blurring, so we can improve our results in a subsequent deblurring step, as shown in [9].

In this paper, we show through analysis and numerical simulations that the resolution estimates derived in [10] extend to finely layered media, with one obvious simplification. Because of the layering, there is no spatial decoherence in the array data, so $X_d = a$, which means that the cross-range resolution can be improved by increasing the array aperture. However, the range resolution remains proportional to $T_d = \frac{\pi}{\Omega_d}$, which is the length of the time window we use to cross-correlate the traces for the purpose of stabilizing our images.

In the scaling regime considered in this paper, the propagation distances in the strongly fluctuating clutter are long and the distance $\pi c_o/B$ traveled over the pulse width π/B covers many layers of size (correlation length) ℓ (π/B of the order of 100ℓ). In this regime there is some averaging and we observe a coherent signal at the array, followed by a long coda. The coherent part of the transmitted pressure field through the layered medium is described by the O’Doherty–Anstey (ODA) theory [24, 12, 1, 18, 16, 5, 31]. ODA predicts that if we observe $P(\vec{x}_r, t)$ in a time window of width $O(\pi/B)$, centered at $\tau(\vec{x}_r, \vec{y})$ plus a small random shift, then we have a deterministic signal which is given by the convolution of the emitted pulse $f(t)$ with a Gaussian. This is known as pulse stabilization, and it is specific to finely layered

media. Naturally, pulse stabilization occurs only at the front of the traces; for later times we have a noisy coda that lasts for a long time.

We shall see that the coherent part of the traces, as described by the ODA theory, gives the leading order term in our imaging functional. This is true for Kirchhoff migration too, which means that $\mathcal{I}^{\text{KM}}(\vec{\mathbf{y}}^s)$ should give fairly well resolved images in layered media. However, these statements should be taken in the asymptotic sense in the limit $\ell B/c_o \rightarrow 0$. In reality, coherent interferometry is a better method because it involves an efficient statistical smoothing and the images are less noisy. This is illustrated clearly by the numerical simulations in section 2.5.

We note also that pulse stabilization is specific to layered media, and since in applications it is unlikely that the clutter is perfectly layered, it is a good idea to work with robust methods, such as coherent interferometry, that are not model dependent.

The paper is organized as follows. In section 2 we formulate the imaging problem for a point source in a finely layered medium. We describe the acoustic equations, the random medium model for the clutter, and the forward model of the acoustic pressure at the array. Then we introduce the coherent interferometric imaging function and compare it, qualitatively and through numerical experiments, to Kirchhoff migration imaging in layered media. In section 3 we specify the scaling and its implications on the statistics of the pressure field recorded at the array. These results are then used in section 4 to derive the coherent interferometric resolution theory in layered media. We end with a summary in section 5.

2. Imaging in finely layered media. Consider the imaging setup shown in Figure 2, where the array lies on a flat surface, parallel to the layers in the medium. Using a system of coordinates with the z -axis normal to the surface of measurements, taken at $z = 0$, we introduce the notation $\vec{\mathbf{x}} = (\mathbf{x}, z)$ that distinguishes the range z from the cross-range $\mathbf{x} \in \mathbb{R}^2$ of an arbitrary point $\vec{\mathbf{x}} \in \mathbb{R}^3$. With this notation, the source is at $\vec{\mathbf{y}} = (\boldsymbol{\xi}, -\eta)$ and the transducer locations are $\vec{\mathbf{x}}_r = (\mathbf{x}_r, 0)$, $r = 1, \dots, N$.

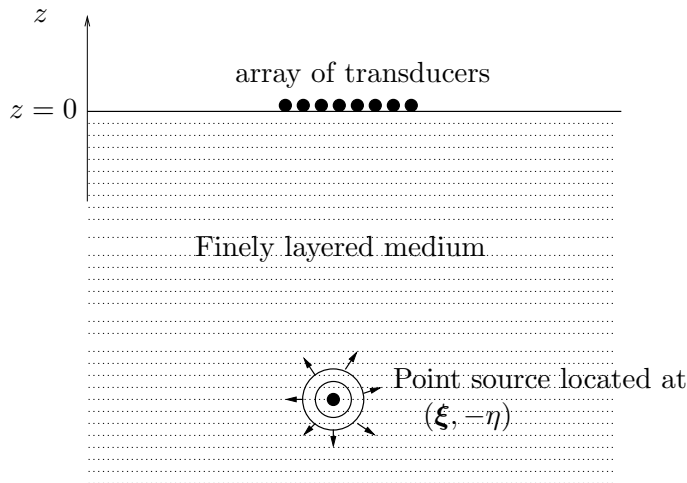


FIG. 2. Setup for recording at transducer locations $\vec{\mathbf{x}}_r$ on the measurement surface $z = 0$, the acoustic waves originating from a point source at $\vec{\mathbf{y}} = (\boldsymbol{\xi}, -\eta)$.

2.1. The forward model for the acoustic pressure at the array. The acoustic wave equations are

$$(2.1) \quad \begin{aligned} \rho \frac{\partial \vec{\mathbf{u}}}{\partial t}(\vec{\mathbf{x}}, t) + \nabla P(\vec{\mathbf{x}}, t) &= \vec{\mathbf{F}}(\vec{\mathbf{x}}, t), \quad \vec{\mathbf{x}} \in \mathbb{R}^3, \quad t > 0, \\ \frac{1}{c^2(z)} \frac{\partial P}{\partial t}(\vec{\mathbf{x}}, t) + \rho \nabla \cdot \vec{\mathbf{u}}(\vec{\mathbf{x}}, t) &= 0, \quad \vec{\mathbf{x}} \in \mathbb{R}^3, \quad t > 0, \\ \vec{\mathbf{u}}(\vec{\mathbf{x}}, t) = \mathbf{0}, \quad P(\vec{\mathbf{x}}, t) &= 0, \quad t < 0, \end{aligned}$$

where $\vec{\mathbf{u}}$ is the velocity of the material particle located at $\vec{\mathbf{x}}$, ρ is the medium density that we suppose is constant, and $c(z)$ is the fluctuating sound speed. The forcing term $\vec{\mathbf{F}}(\vec{\mathbf{x}}, t)$ is due to the point source at $\vec{\mathbf{y}}$ that emits pulse (1.1) in the vertical, upward direction $\vec{\mathbf{e}}_3$, so we set

$$(2.2) \quad \vec{\mathbf{F}}(\vec{\mathbf{x}}, t) = f(t)\delta(\vec{\mathbf{x}} - \vec{\mathbf{y}})\vec{\mathbf{e}}_3.$$

The clutter is contained in the half space $z < 0$ and is modeled as

$$(2.3) \quad \frac{1}{c^2(z)} = \frac{1}{c_o^2} \left[1 + \sigma \nu \left(\frac{z}{\ell} \right) \right], \quad z \in (-L, 0),$$

where ν is a random, stationary process with mean zero and rapidly decaying covariance

$$(2.4) \quad \mathcal{C}(z_1 - z_2) = E \{ \nu(z_1) \nu(z_2) \}$$

satisfying

$$(2.5) \quad \mathcal{C}(0) = 1, \quad \int_{-\infty}^{\infty} \mathcal{C}(z) dz = 1,$$

so that ℓ in (2.3) is a correlation length. The parameter σ quantifies the strength of the fluctuations. We consider here strong fluctuations $\sigma \sim 1$ and a high frequency regime; i.e., the wavelength covers many correlation lengths $\ell \ll \lambda_o$. In principle, the clutter can extend to the whole half space $z < 0$, but the hyperbolicity of the problem and the finite time window over which we record the traces imply that we will not see the effect of the layers below some finite depth L , so we may as well restrict the random medium to the strip $(-L, 0)$. For z outside the strip, we set $c = c_o$.

Equations (2.1) can be transformed easily to a system of ODEs in the z variable by Fourier transforming in \mathbf{x} and t . This leads to the solution [24, 13, 12, 25, 1, 18, 16, 31, 21, 20]

$$(2.6) \quad P(\vec{\mathbf{x}}, t) = \frac{1}{2\pi} \int_{|\omega - \omega_0| \leq B} d\omega \hat{P}(\vec{\mathbf{x}}, \omega) e^{-i\omega t},$$

for an arbitrary point $\vec{\mathbf{x}} = (\mathbf{x}, 0)$ on the surface of measurements, where

$$(2.7) \quad \begin{aligned} \hat{P}(\vec{\mathbf{x}}, \omega) &= \frac{\omega^2 \hat{f}_B(\omega - \omega_0)}{8\pi^2} \int d\boldsymbol{\kappa} \left\{ \mathcal{T}(\omega, \boldsymbol{\kappa}_z) e^{i\omega(\boldsymbol{\kappa}, \boldsymbol{\kappa}_z) \cdot (\mathbf{x} - \boldsymbol{\xi}, \eta)} \right. \\ &\quad \left. + \mathcal{R}(\omega, \boldsymbol{\kappa}_z) e^{i\omega(\boldsymbol{\kappa}, \boldsymbol{\kappa}_z) \cdot (\mathbf{x} - \boldsymbol{\xi}, -\eta)} \right\} \end{aligned}$$

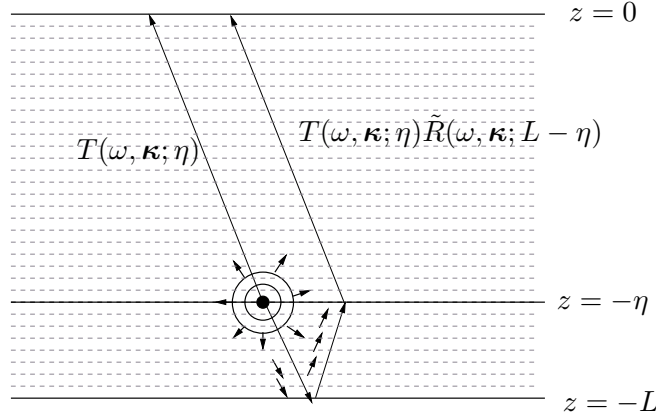


FIG. 3. Schematic of the first terms in the series (2.9) of \mathcal{T} and \mathcal{R} . $T(\omega, \kappa; \eta)$ gives the amplitude of the total transmitted field that goes from the source to the array at the top. $T(\omega, \kappa; \eta)\tilde{R}(\omega, \kappa; L - \eta)$ accounts for the full scattered field reflected from the layer $(-L, -\eta)$ below the source. $\tilde{R}(\omega, \kappa; L - \eta)$ is the upgoing reflection coefficient from the layer $(-L, -\eta)$ at the level $z = -\eta$.

is the superposition of plane waves traveling along direction $\vec{\kappa} = (\kappa, \kappa_z)$, with κ and κ_z being the lateral and vertical slownesses, respectively. The plane wave decomposition is done with respect to the background medium, of constant slowness c_o^{-1} , so that

$$(2.8) \quad |\kappa|^2 + \kappa_z^2 = c_o^{-2} \quad \text{and} \quad \kappa_z = \frac{\sqrt{1 - c_o^2 \kappa^2}}{c_o}, \quad \text{where} \quad \kappa^2 = |\kappa|^2.$$

The effect of the random medium on $P(\vec{x}, t)$ is encoded in the coefficients $\mathcal{T}(\omega, \kappa_z)$ and $\mathcal{R}(\omega, \kappa_z)$ that account for multiple reflections of the waves by the layers. Explicitly, if we let $T(\omega, \kappa_z; \eta)$ and $R(\omega, \kappa_z; \eta)$ be the transmission and reflection coefficients of the random medium occupying the interval $z \in (-\eta, 0)$ and $\tilde{R}(\omega, \kappa_z; L - \eta)$ be the reflection coefficient of the random medium in $z \in (-L, -\eta)$, we have [21, 20]

$$(2.9) \quad \begin{aligned} \mathcal{T}(\omega, \kappa_z) &= T(\omega, \kappa_z; \eta) \sum_{n=0}^{\infty} R^n(\omega, \kappa_z; \eta) \tilde{R}^n(\omega, \kappa_z; L - \eta), \\ \mathcal{R}(\omega, \kappa_z) &= T(\omega, \kappa_z) \tilde{R}(\omega, \kappa_z; L - \eta). \end{aligned}$$

A schematic describing the first terms in \mathcal{T} and \mathcal{R} is given in Figure 3. The interpretation of the next terms follows easily, as increasing n in (2.9) accounts for multiple reflections from the layer $(-L, -\eta)$ at $z = -\eta$. The reflection coefficient $\tilde{R}(\omega, \kappa_z; L - \eta)$ gives the upgoing field from the layer $(-L, -\eta)$ at the level $z = -\eta$ and $R(\omega, \kappa_z; \eta)$ is the downgoing reflection coefficient from the layer $(-\eta, 0)$ at the level $z = -\eta$. Note that $\mathcal{R}(\omega, \kappa_z)$ differs from $\mathcal{T}(\omega, \kappa_z)$ by an extra reflection caused by the layer $(-L, -\eta)$ at the level $z = -\eta$.

2.2. The coherent pressure field. In the absence of the fluctuations, $\mathcal{T}(\omega, \kappa_z) = 1$, $\mathcal{R} = 0$, and (2.6), (2.7) reduce to

$$(2.10) \quad \begin{aligned} P_o(\vec{x}, t) &= \int_{|\omega - \omega_0| \leq B} d\omega \frac{\omega^2 \hat{f}_B(\omega - \omega_0)}{2(2\pi)^3} \int d\kappa e^{i\omega(\kappa, \kappa_z) \cdot (\mathbf{x} - \xi, \eta) - i\omega t} \\ &= \frac{\partial}{\partial z} \left\{ \frac{f(t - \tau((\mathbf{x}, z), \vec{y}))}{4\pi |(\mathbf{x}, z) - \vec{y}|} \right\}_{z=0}, \end{aligned}$$

where

$$(2.11) \quad \tau(\vec{\mathbf{x}}, \vec{\mathbf{y}}) = |\vec{\mathbf{x}} - \vec{\mathbf{y}}|/c_o$$

is the travel time in the homogeneous medium. Thus, each trace $P_o(\vec{\mathbf{x}}_r, t)$ has a blip centered at $t = \tau(\vec{\mathbf{x}}_r, t)$, of width $O(\pi/B)$, for $r = 1, \dots, N$.

In the cluttered medium the traces are noisy (see, for example, Figure 9), but if we look at their expectation we obtain formula [24, 13, 12, 25, 1, 18, 16, 31]

$$(2.12) \quad E\{P(\vec{\mathbf{x}}, t)\} \approx \frac{\partial}{\partial z} \left\{ \frac{(f \star \tilde{\mathcal{N}})(t - \tau((\mathbf{x}, z), \vec{\mathbf{y}}))}{4\pi|(\mathbf{x}, z) - \vec{\mathbf{y}}|} \right\}_{z=0},$$

which is similar to (2.10), except for the convolution of the pulse with Gaussian

$$(2.13) \quad \tilde{\mathcal{N}}(t) = \frac{\sin \theta(\mathbf{x})}{2\sqrt{\pi}T_{\text{ps}}} e^{-\frac{t^2 \sin^2 \theta(\mathbf{x})}{4T_{\text{ps}}^2}}, \quad \sin \theta(\mathbf{x}) = \frac{\eta}{|\vec{\mathbf{x}} - \vec{\mathbf{y}}|}.$$

The many reflections in the clutter lead to a diffusion or a spreading of the pulse, quantified by T_{ps} , a clutter dependent parameter with units of time. Note that T_{ps} is the same across the array, but the pulse spreading is more severe for waves propagating at shallow angles $\theta(\mathbf{x})$.

When we image, we have only traces from a single cluttered environment. We cannot, therefore, observe the expected field (2.12). However, in the regime considered here (see section 3), the size of the layers is small compared to the distance $\pi c_o/B$ covered by the width of the pulse, and some averaging occurs to give us a coherent front that can be observed in a time window of size $O(\pi/B)$, centered at the deterministic arrival time, plus a small time shift. This coherent front is described by the ODA formula [24, 13, 12, 25, 1, 18, 16, 31] which predicts that, in the asymptotic limit $\ell B/c_o \rightarrow 0$, we have for time window $|t - \tau((\mathbf{x}, z), \vec{\mathbf{y}})| \leq O(\pi/B)$,

$$(2.14) \quad P(\vec{\mathbf{x}}, t) \approx \frac{\partial}{\partial z} \left\{ \frac{(f \star \mathcal{N})(t - \tau((\mathbf{x}, z), \vec{\mathbf{y}}) - \delta\tau(\mathbf{x}))}{4\pi|(\mathbf{x}, z) - \vec{\mathbf{y}}|} \right\}_{z=0}, \quad \mathcal{N}(t) = \frac{\sin \theta(\mathbf{x})}{\sqrt{2\pi}T_{\text{ps}}} e^{-\frac{t^2 \sin^2(\theta(\mathbf{x}))}{2T_{\text{ps}}^2}},$$

where $\delta\tau$ is a random time shift given by

$$(2.15) \quad \delta\tau(\mathbf{x}) = \frac{T_{\text{ps}}}{\sin \theta(\mathbf{x})} \frac{W(\eta)}{\sqrt{\eta}}.$$

Here $W(\eta)$ is a standard Brownian motion. Note that the pulse spread in the ODA formula (2.14) is half of what we had in (2.12). This is due to the random time shift (2.15) that gives smearing when averaging P over different realizations of the medium, which doubles the expected pulse spread.

Because (2.14) describes approximately the coherent part of the pressure recorded at the array, it represents the ideal object to use in imaging. Thus, if we could separate the coherent front of the traces from the coda, we could image with any deterministic method and obtain a good image, up to a small random shift. Moreover, we could use formula (2.15) and the array to eliminate the random shift and improve the accuracy of the image [22]. However, such a method is model dependent, because it relies heavily on the accuracy of the ODA formula, and it is also difficult to generalize to more interesting problems of imaging distributed sources or scatterers, where coherent

arrivals coming from greater depths are hidden in the coda of signals originating closer to the array.

In the next two sections we discuss the point spread function of two imaging methods: Kirchhoff migration and coherent interferometry. Then we compare their performance with numerical simulations in section 2.5.

2.3. Kirchhoff migration. As explained in the introduction, Kirchhoff migration imaging function (1.1) works well when the clutter is weak and there is no significant delay spread in the traces recorded at the array. We consider a square array centered at $\vec{\mathbf{x}}_c = (\mathbf{x}_c, 0)$, with aperture $a \ll |\vec{\mathbf{x}}_c - \vec{\mathbf{y}}|$, where the range and direction of arrival resolution limits [7, 10] are

$$(2.16) \quad \left| |\vec{\mathbf{x}}_c - \vec{\mathbf{y}}| - |\vec{\mathbf{x}}_c - \vec{\mathbf{y}}^s| \right| \leq O\left(\frac{\pi c_o}{B}\right), \quad \left| \frac{\mathbf{x}_c - \boldsymbol{\xi}}{|\vec{\mathbf{x}}_c - \vec{\mathbf{y}}|} - \frac{\mathbf{x}_c - \boldsymbol{\xi}^s}{|\vec{\mathbf{x}}_c - \vec{\mathbf{y}}^s|} \right| \leq O\left(\frac{\pi c_o}{Ba}\right).$$

Here $\vec{\mathbf{y}}^s = (\boldsymbol{\xi}^s, -\eta^s)$ is the search point. Furthermore, if the remote array is located nearly above the source, $|\mathbf{x}_c - \boldsymbol{\xi}| \ll \eta$ and (2.16) reduces to

$$(2.17) \quad |\eta - \eta^s| \leq O\left(\frac{\pi c_o}{B}\right), \quad |\boldsymbol{\xi} - \boldsymbol{\xi}^s| \leq O\left(\frac{\pi c_o \eta}{Ba}\right).$$

When there is significant multiple scattering due to clutter, Kirchhoff migration is known to not work well, because the traces are noisy and by migrating them to the search point $\vec{\mathbf{y}}^s$, with the deterministic travel times (2.11), we cannot compress the delay spread in $P(\vec{\mathbf{x}}_r, t)$, $r = 1, \dots, N$. There is some averaging in Kirchhoff migration, because of the summation over the array, but usually this is not enough, so the results are noisy and they change unpredictably with the realizations of the clutter. This is illustrated in [8, 10, 9] for isotropic clutter.

In finely layered media, where the pulse width covers many correlation lengths, we have pulse stabilization [24, 13, 12, 25, 1, 18, 16, 31], so Kirchhoff migration should work, in principle. Ideally, we should expect resolution limits similar to (2.17), except for the replacement of the bandwidth B by a shorter one, B_{ps} , due to the pulse spread in the ODA formula (2.14). The random arrival time (2.15) affects the resolution as well, because receivers that are at a smaller angle $\theta(\mathbf{x})$ perceive a longer time shift than the ones that sit on top of the target, so the image will be smeared to some degree. This latter effect should be small, however, for small array apertures.

It may be surprising at first that, even for traces recorded in a long time window that contains mostly coda, only the ODA formula plays a role in imaging. We explain this in section 3. In short, we show there that in the asymptotic limit $\ell B/c_o \rightarrow 0$ and $c_o/(B\eta) \rightarrow 0$, such that $\ell\eta \sim (c_o/B)^2$, the reflection coefficients in (2.9) decorrelate rapidly in the frequency and vertical slowness κ_z , and, subsequently, that $\mathcal{I}^{\text{KM}}(\vec{\mathbf{y}}^s)$ converges weakly, in probability, to the imaging function with the ODA formula. Of course, this is an asymptotic result. In practice, the coda is felt to some degree in Kirchhoff migration and the images are somewhat noisy, as illustrated in the numerical experiments of section 2.5. The noise should be even more visible in media that are not perfectly layered and in other scaling regimes.

2.4. Coherent interferometry. The coherent interferometric imaging function is

$$(2.18) \quad \mathcal{I}^{\text{CINT}}(\vec{\mathbf{y}}^s, \Omega_d) = \sum_{r=1}^N \sum_{r'=1}^N \int d\omega \int_{|\omega - \omega'| \leq \Omega_d} d\omega' \widehat{P}(\vec{\mathbf{x}}_r, \omega) \overline{\widehat{P}(\vec{\mathbf{x}}_{r'}, \omega')} e^{-i\omega\tau(\vec{\mathbf{x}}_r, \vec{\mathbf{y}}^s) + i\omega'\tau(\vec{\mathbf{x}}_{r'}, \vec{\mathbf{y}}^s)},$$

where we restrict the domain of integration over the frequencies by the parameter $\Omega_d < B$, which plays a key role in clutter because it allows an efficient statistical smoothing [28] of the images, as we show next.

Denote by $\hat{\chi}(\omega)$ the window function supported in the interval $[-\Omega_d, \Omega_d]$ and introduce the central and difference frequency variables

$$(2.19) \quad \bar{\omega} = \frac{\omega + \omega'}{2}, \quad \tilde{\omega} = \omega - \omega',$$

to rewrite (2.18) as

$$(2.20) \quad \begin{aligned} \mathcal{I}^{\text{CINT}}(\vec{\mathbf{y}}^s, \Omega_d) &= \sum_{r=1}^N \sum_{r'=1}^N \int d\bar{\omega} \int d\tilde{\omega} \hat{\chi}(\tilde{\omega}) \hat{P} \left(\vec{\mathbf{x}}_r, \bar{\omega} + \frac{\tilde{\omega}}{2} \right) \overline{\hat{P} \left(\vec{\mathbf{x}}_{r'}, \bar{\omega} - \frac{\tilde{\omega}}{2} \right)} \\ &\times \exp \left\{ -i\bar{\omega} [\tau(\vec{\mathbf{x}}_r, \vec{\mathbf{y}}^s) - \tau(\vec{\mathbf{x}}_{r'}, \vec{\mathbf{y}}^s)] - i\frac{\tilde{\omega}}{2} [\tau(\vec{\mathbf{x}}_r, \vec{\mathbf{y}}^s) + \tau(\vec{\mathbf{x}}_{r'}, \vec{\mathbf{y}}^s)] \right\}. \end{aligned}$$

Undoing the Fourier transforms in (2.20), we obtain after simple algebraic manipulations

$$(2.21) \quad \begin{aligned} \mathcal{I}^{\text{CINT}}(\vec{\mathbf{y}}^s, \Omega_d) &\sim \sum_{r=1}^N \sum_{r'=1}^N \int d\bar{t} \int d\tilde{t} P \left(\vec{\mathbf{x}}_r, \bar{t} + \frac{\tilde{t}}{2} \right) P \left(\vec{\mathbf{x}}_{r'}, \bar{t} - \frac{\tilde{t}}{2} \right) \\ &\times \delta_B \left[\bar{t} - \tau(\vec{\mathbf{x}}_r, \vec{\mathbf{y}}^s) + \tau(\vec{\mathbf{x}}_{r'}, \vec{\mathbf{y}}^s) \right] \chi \left[\frac{\tau(\vec{\mathbf{x}}_r, \vec{\mathbf{y}}^s) + \tau(\vec{\mathbf{x}}_{r'}, \vec{\mathbf{y}}^s)}{2} - \bar{t} \right], \end{aligned}$$

where the symbol \sim stands for approximate equality up to a multiplicative constant, χ is the inverse Fourier transform of the window function $\hat{\chi}$, and

$$(2.22) \quad \begin{aligned} \delta_B \left[\bar{t} - \tau(\vec{\mathbf{x}}_r, \vec{\mathbf{y}}^s) + \tau(\vec{\mathbf{x}}_{r'}, \vec{\mathbf{y}}^s) \right] &= \int_{|\bar{\omega} - \omega_0| \leq B} \frac{d\bar{\omega}}{2\pi} \exp \left\{ i\bar{\omega} \left[\bar{t} - \tau(\vec{\mathbf{x}}_r, \vec{\mathbf{y}}^s) + \tau(\vec{\mathbf{x}}_{r'}, \vec{\mathbf{y}}^s) \right] \right\} \\ &= e^{i\omega_0 \left[\bar{t} - \tau(\vec{\mathbf{x}}_r, \vec{\mathbf{y}}^s) + \tau(\vec{\mathbf{x}}_{r'}, \vec{\mathbf{y}}^s) \right]} \frac{\sin \left\{ B \left[\bar{t} - \tau(\vec{\mathbf{x}}_r, \vec{\mathbf{y}}^s) + \tau(\vec{\mathbf{x}}_{r'}, \vec{\mathbf{y}}^s) \right] \right\}}{\pi \left[\bar{t} - \tau(\vec{\mathbf{x}}_r, \vec{\mathbf{y}}^s) + \tau(\vec{\mathbf{x}}_{r'}, \vec{\mathbf{y}}^s) \right]} \end{aligned}$$

is an approximate delta function, for large bandwidth B .

The expression (2.21) shows that for $B \rightarrow \infty$,

$$(2.23) \quad \mathcal{I}^{\text{CINT}}(\vec{\mathbf{y}}^s, \Omega_d) \sim \mathcal{J}(\vec{\mathbf{y}}^s, \bar{t}) \star \chi(\bar{t}) \Big|_{\bar{t} = \frac{\tau(\vec{\mathbf{x}}_r, \vec{\mathbf{y}}^s) + \tau(\vec{\mathbf{x}}_{r'}, \vec{\mathbf{y}}^s)}{2}},$$

where

$$(2.24) \quad \mathcal{J}(\vec{\mathbf{y}}^s, \bar{t}) = \sum_{r=1}^N \sum_{r'=1}^N P \left[\vec{\mathbf{x}}_r, \bar{t} + \frac{\tau(\vec{\mathbf{x}}_r, \vec{\mathbf{y}}^s) - \tau(\vec{\mathbf{x}}_{r'}, \vec{\mathbf{y}}^s)}{2} \right] P \left[\vec{\mathbf{x}}_{r'}, \bar{t} - \frac{\tau(\vec{\mathbf{x}}_r, \vec{\mathbf{y}}^s) - \tau(\vec{\mathbf{x}}_{r'}, \vec{\mathbf{y}}^s)}{2} \right]$$

and the symbol \star denotes convolution. Because

$$(2.25) \quad \mathcal{J} \left[\vec{\mathbf{y}}^s, \frac{\tau(\vec{\mathbf{x}}_r, \vec{\mathbf{y}}^s) + \tau(\vec{\mathbf{x}}_{r'}, \vec{\mathbf{y}}^s)}{2} \right] = [\mathcal{I}^{\text{KM}}(\vec{\mathbf{y}}^s)]^2,$$

the expression (2.23) is a smoothed version of $[\mathcal{I}^{\text{KM}}(\vec{\mathbf{y}}^s)]^2$, where the fluctuations in the Kirchhoff migration image are diminished by the convolution with the window χ , so as to give a stable but blurred estimate of the source location. Naturally, the smoothing comes at the expense of resolution. We analyze in detail the resolution of $\mathcal{I}^{\text{CINT}}(\vec{\mathbf{y}}^s, \Omega_d)$ in section 4. Here we give a heuristic estimate using (2.21).

We begin by assuming as in the previous section that the array is small and centered at $\vec{\mathbf{x}}_c$, and we approximate

$$(2.26) \quad \begin{aligned} \tau(\vec{\mathbf{x}}_r, \vec{\mathbf{y}}^s) - \tau(\vec{\mathbf{x}}_{r'}, \vec{\mathbf{y}}^s) &\approx \tilde{\mathbf{x}} \cdot \nabla_{\mathbf{x}} \tau((\bar{\mathbf{x}}, 0), \vec{\mathbf{y}}^s) \approx \tilde{\mathbf{x}} \cdot \nabla_{\mathbf{x}} \tau(\vec{\mathbf{x}}_c, \vec{\mathbf{y}}^s), \\ \frac{\tau(\vec{\mathbf{x}}_r, \vec{\mathbf{y}}^s) + \tau(\vec{\mathbf{x}}_{r'}, \vec{\mathbf{y}}^s)}{2} &\approx \tau((\bar{\mathbf{x}}, 0), \vec{\mathbf{y}}^s) \approx \tau(\vec{\mathbf{x}}_c, \vec{\mathbf{y}}^s), \end{aligned}$$

for central and difference locations $\bar{\mathbf{x}} = (\mathbf{x}_r + \mathbf{x}_{r'})/2$, $\tilde{\mathbf{x}} = \mathbf{x}_r - \mathbf{x}_{r'}$ spanning the array \mathcal{A} , as r, r' vary in $1, \dots, N$. Now recall (2.22) and that χ is supported in interval π/Ω_d , to obtain roughly

$$(2.27) \quad \begin{aligned} \mathcal{I}^{\text{CINT}}(\vec{\mathbf{y}}^s, \Omega_d) &\sim \sum_{\bar{\mathbf{x}} \in \mathcal{A}} \sum_{|\tilde{\mathbf{x}}| \leq a} \int_{|\bar{t} - \tau(\vec{\mathbf{x}}_c, \vec{\mathbf{y}}^s)| \leq \pi/\Omega_d} d\bar{t} \int_{|\bar{t} - \tilde{\mathbf{x}} \cdot \nabla_{\mathbf{x}} \tau(\vec{\mathbf{x}}_c, \vec{\mathbf{y}}^s)| \leq \pi/B} d\tilde{t} \\ &\quad \times P\left(\bar{t} + \frac{\tilde{t}}{2}, (\bar{\mathbf{x}} + \frac{\tilde{\mathbf{x}}}{2}, 0)\right) P\left(\bar{t} - \frac{\tilde{t}}{2}, (\bar{\mathbf{x}} - \frac{\tilde{\mathbf{x}}}{2}, 0)\right). \end{aligned}$$

The resolution estimates follow from (2.27) and the results in section 2.2. The uncertainty in range comes from the integration over \bar{t} , which extends to an interval of length π/Ω_d . The uncertainty in the direction of arrival $c_o \nabla_{\mathbf{x}} \tau(\vec{\mathbf{x}}_c, \vec{\mathbf{y}})$ comes from the integration over the time lag \tilde{t} . Since $|\tilde{\mathbf{x}}| \leq a$, we have $|\nabla_{\mathbf{x}} \tau(\vec{\mathbf{x}}_c, \vec{\mathbf{y}}^s)| \leq \pi/(Ba)$ and the resolution limits are

$$(2.28) \quad \|\vec{\mathbf{x}}_c - \vec{\mathbf{y}}\| - \|\vec{\mathbf{x}}_c - \vec{\mathbf{y}}^s\| \leq O\left(\frac{\pi c_o}{\Omega_d}\right), \quad \left| \frac{\mathbf{x}_c - \boldsymbol{\xi}}{\|\vec{\mathbf{x}}_c - \vec{\mathbf{y}}\|} - \frac{\mathbf{x}_c - \boldsymbol{\xi}^s}{\|\vec{\mathbf{x}}_c - \vec{\mathbf{y}}^s\|} \right| \leq O\left(\frac{\pi c_o}{Ba}\right).$$

We show in section 4 that estimates (2.28) are correct, except for the replacement of the bandwidth by B_{ps} , a smaller value than B due to the pulse spreading that occurs in finely layered media. In any case, we note a delicate balance between the smoothing effect of Ω_d and the resolution. The smaller that Ω_d is, the smoother the image but the worse the resolution. It is difficult to find the optimal Ω_d from the theory of wave propagation in finely layered media. However, we can estimate it from the image itself, as shown in [9] and in the next section.

2.5. Numerical simulations. We present in this section the results of numerical simulation for imaging both with Kirchhoff migration and with the coherent interferometric functional. The setup for the numerical experiments is shown in Figure 4, where the dimensions of the problem are given in terms of the central wavelength λ_0 . We use an array of 41 transducers at a distance $h = \lambda_0/2$ from each other. The object (the source) to be imaged is at range $L = 78\lambda_0$ and at zero cross-range, measured with respect to the center of the array. To obtain the numerical point spread function of the imaging functionals, we consider first the case of imaging a point source. Then we illustrate the robustness of the coherent interferometric array imaging (CINT) functional with a more complicated extended source, consisting of four point sources emitting simultaneously the same pulse $f(t)$. The pulse $f(t)$ is the time derivative of a Gaussian with central frequency $\omega_0/(2\pi) = 1\text{kHz}$ and bandwidth $0.6 - 1.3\text{kHz}$

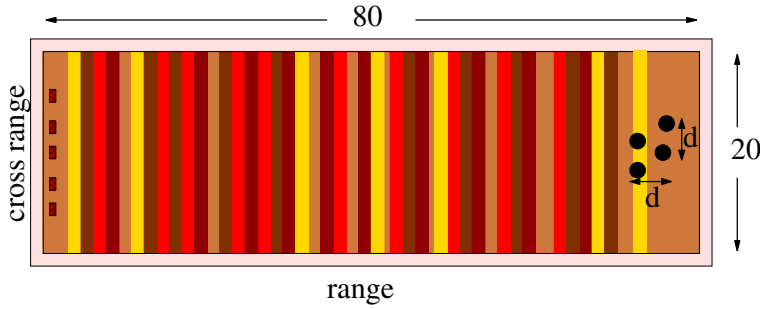


FIG. 4. *The setup for the numerical simulations. We show in this figure the extended source, consisting of four point sources located at $(74, 0)$, $(74, 4)$, $(78, 2)$, $(78, -2)$. The units are in carrier wavelengths λ_o and the distance d is 4. The array has 41 transducers at a distance $h = \lambda_o/2$ apart, with the central transducer located at point $(0, 2)$.*

(measured at 6dB). In the following simulations the mean of the propagation speed is 3km/s, and so the central wavelength is $\lambda_0 = 3\text{m}$.

The background randomly layered medium shown in Figure 4 is only schematic. Two realizations of the actual randomly layered medium used in the simulations are shown in Figure 5. The sound speed is given by (2.3) with mean $c_0 = 3.0\text{Km/s}$ and where the random, stationary process $\nu(\frac{z}{l})$ is modeled using random Fourier series and a Gaussian correlation function. The correlation length is $l = 30\text{cm}$ and the standard deviation is $\sigma = 30\%$.

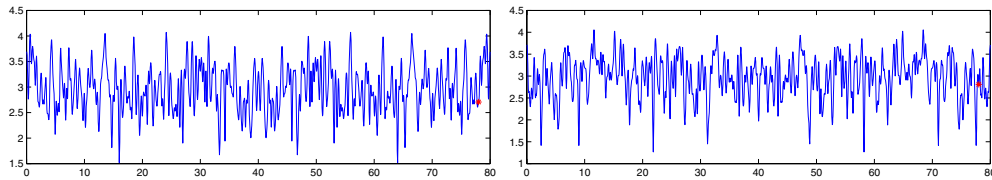


FIG. 5. *Two realizations of the randomly layered medium, with a source at the location indicated by a star. The abscissa units are in carrier wavelength λ_o and the sound speed is measured in km/s.*

To generate the array data we solve the acoustic wave equation, formulated as a first order in time velocity-pressure system (2.1), using a mixed finite element method [2, 3]. The propagation medium is considered to be infinite in all directions, and in the numerical computations a perfectly matched absorbing layer surrounds the domain [4]. In Figure 6 we show numerically generated time traces recorded at the array for one realization of the layered medium (in Figure 5 (left)) and the two sources configurations considered.

The images obtained with these data using the coherent interferometric functional are presented in Figures 7–8, where they are also compared with images obtained using Kirchhoff migration. We note that the CINT images are smoother and more stable than the ones obtained with Kirchhoff migration, as the theory suggests. This can be seen by looking at the results close to the source location where the image corresponds to the point spread function of the imaging functional. What the resolution theory cannot predict are the “ghost” reconstructed sources that we observe both in coherent interferometry and in Kirchhoff migration. These are due to the echoes from some particular layers and their location changes for different realizations of the random medium (compare the left and right column in Figure 7).

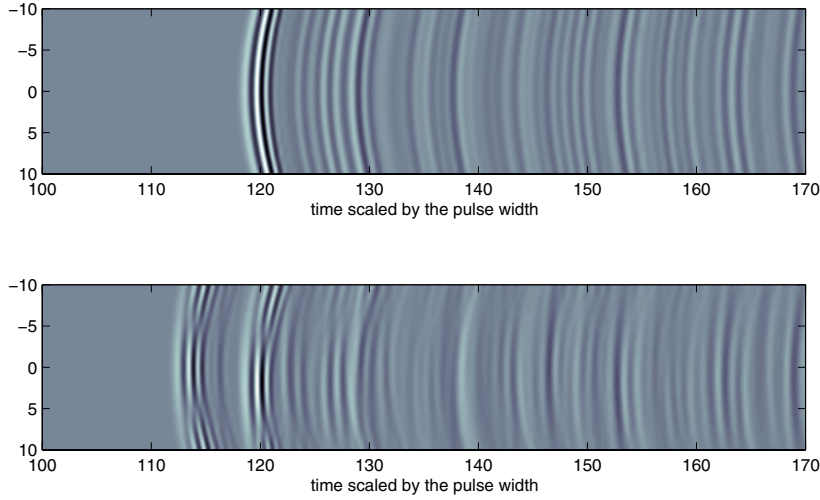


FIG. 6. *Traces recorded at the array for a single source (top) and four sources (bottom) buried in the randomly layered medium shown in Figure 5 (left).*

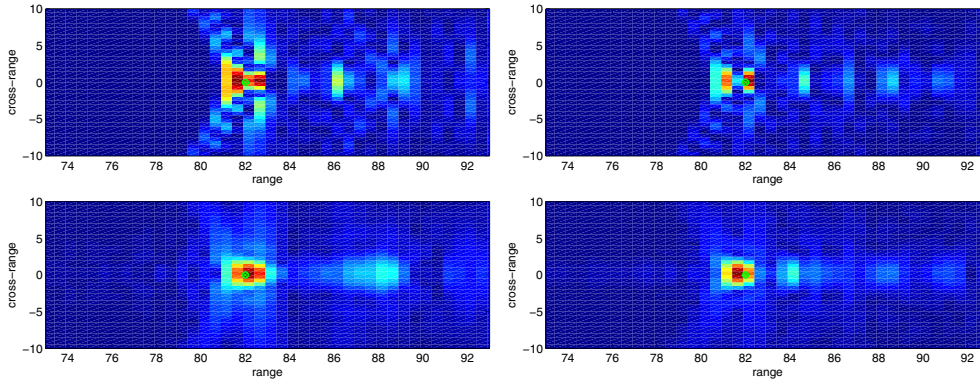


FIG. 7. *Top: Kirchhoff migration images of a single source for the two realizations of the random medium shown in Figure 5. The image on the left (resp., right) corresponds to the random medium shown in Figure 5 (left) (resp., Figure 5 (right)). Bottom: Coherent interferometric images of the same source for the same two realizations of the background layered medium. The correct location of the source is shown in each figure with a big dot.*

In the case of one point source, we note that the images obtained with Kirchhoff migration are slightly more noisy than the ones obtained with coherent interferometry. However, one can argue that this does not really affect the estimate of the location of the source. The important observation here is that when the point spread function of the imaging method is noisy, this will affect the resolution of the images for extended objects and therefore make the method less reliable for imaging in clutter. To illustrate this we consider the example with the four sources shown in Figure 4. The results obtained with coherent interferometry and Kirchhoff migration are shown in Figure 8. Clearly, with coherent interferometry the four sources can be reconstructed, while the sources in the back are lost in the noise for Kirchhoff migration.

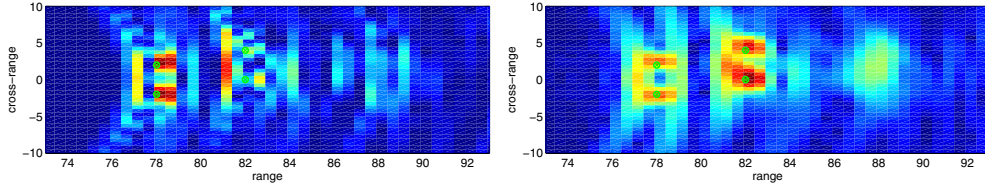


FIG. 8. *Left: Kirchhoff migration image of four sources in the random medium shown in Figure 5 (left). The traces recorded at the array are shown in Figure 6 (bottom). Right: Coherent interferometric image of the same sources in the same medium. The correct location of the sources is indicated with big dots.*

REMARK 1. As pointed out in section 2.4 there is a trade-off between stability and resolution, expressed here through the choice of the parameter Ω_d . This parameter is adaptively estimated using information from the reconstructed image (cf. [9]). To measure the quality of the reconstruction we compute the total variation (TV; see [29]) norm of the image (L_1 plus L_1 of the gradient) and we choose the parameter Ω_d as the one which minimizes this norm. The choice of the TV norm is based on the following considerations. First, using the L_1 norm of the image is consistent with our objective to minimize the image support or, in other words, to have a sparse representation that reduces the blurring. Second, the L_1 norm of the gradient expresses our objective to penalize the noise by minimizing rapid oscillations in the image. We do not claim that minimizing the TV norm is the best possible choice. It is, however, the one that gives the best results among the various methods we tried (including the Shannon entropy method; see [30]). In the examples presented here, $\Omega_d = B/6$ for the first realization of the layered medium and $\Omega_d = B/4$ for the second one.

REMARK 2. In the reconstructed images the source positions are shifted in range by approximately $4\lambda_0$. This corresponds to the random shift predicted by the ODA theory. The shift seems to be constant along the array elements in these experiments, as the array aperture is small compared to the range. Different shifts are observed for different realizations of the layered medium. The pulse spreading as a function of depth is illustrated in Figure 9. At depth $78\lambda_0$, corresponding to the source position, the width of the pulse is approximately double the initial one.

3. The scaling and statistics of the recorded pressure field. There are three important length scales in this problem: the propagation distance $O(\eta)$, the correlation length ℓ of the fluctuations, and the distance $\pi c_o/B$ traveled by the pulse of width π/B . We consider a high frequency regime

$$(3.1) \quad \lambda_o = O\left(\frac{\pi c_o}{B}\right) \ll \eta,$$

and we set

$$(3.2) \quad \frac{\lambda_o}{\eta} = \epsilon \ll 1.$$

The fluctuations are strong $\sigma \sim 1$ (see (2.3)), but the wavelengths cover many correlation lengths

$$(3.3) \quad \ell \ll \frac{\pi c_o}{B} \sim \lambda_o,$$

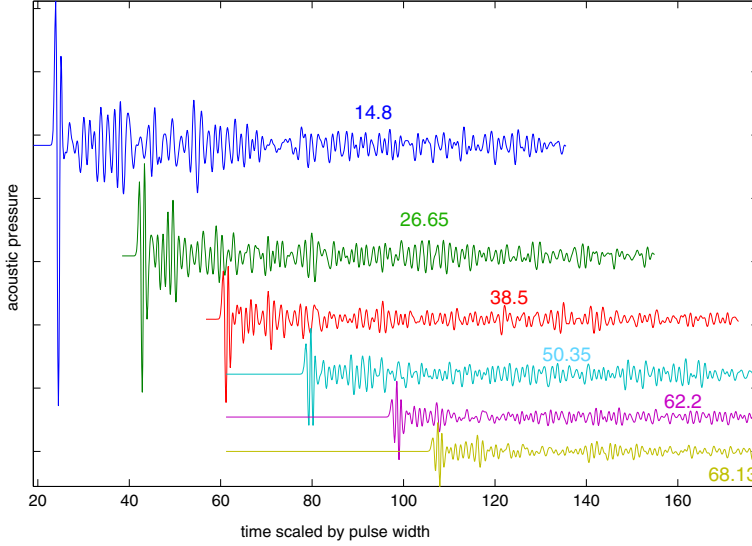


FIG. 9. *Traces recorded at a fixed transducer in the array for a single source buried at different depths (the distance from the array is indicated in units of central wavelength λ_o) in the layered medium shown in Figure 5 (left).*

so some averaging of the wave field occurs and we can get a coherent front at the array. This averaging is done through a diffusion limit [26, 27, 1, 23], which requires that (3.1) and (3.3) be related by

$$(3.4) \quad \ell\eta = O\left(\frac{\pi c_o}{B}\right)^2.$$

We can then set the scaled range η to be $O(1)$ relative to ϵ , which means that the scaled wavelengths should be proportional to ϵ and the scaled correlation length proportional to ϵ^2 . This ϵ scaling implies that the probing pulse has the form

$$(3.5) \quad f(t) = e^{-i\frac{\omega_0}{\epsilon}t} f_{\frac{B}{\epsilon}}\left(\frac{t}{\epsilon}\right),$$

with bandwidth B/ϵ . The forward model (2.6), (2.7) becomes

$$(3.6) \quad P(\vec{x}, t) = \int_{|\omega - \omega_0| \leq B} d\omega \frac{\omega^2 \widehat{f}_B(\omega - \omega_0)}{2(2\pi\epsilon)^3} \int d\kappa \left\{ \mathcal{T}\left(\frac{\omega}{\epsilon}, \kappa_z\right) e^{i\frac{\omega}{\epsilon}(\kappa, \kappa_z) \cdot (\mathbf{x} - \xi, \eta)} \right. \\ \left. + \mathcal{R}\left(\frac{\omega}{\epsilon}, \kappa_z\right) e^{i\frac{\omega}{\epsilon}(\kappa, \kappa_z) \cdot (\mathbf{x} - \xi, 2L - \eta)} \right\}.$$

Finally, we scale the smoothing parameter Ω_d as

$$(3.7) \quad \Omega_d \rightsquigarrow \frac{\Omega_d}{\epsilon},$$

and expect that $\Omega_d \ll B$, for some smoothing to take place. If $\Omega_d \sim B$, the coherent interferometric function essentially becomes $[\mathcal{I}^{\text{KM}}(\vec{y}^s)]^2$ and no smoothing occurs.

3.1. The asymptotic characterization of the recorded pressure field.

The statistics of the pressure field (3.6) are studied in detail in [24, 13, 12, 25, 1, 18, 16, 31, 21, 20] in the asymptotic limit $\epsilon \rightarrow 0$. Since the effect of the random medium on $P(t, \vec{x})$ is encoded in coefficients \mathcal{T} and \mathcal{R} , which in turn depend on $T\left(\frac{\omega}{\epsilon}, \kappa_z; \eta\right)$, $R\left(\frac{\omega}{\epsilon}, \kappa_z; \eta\right)$, and $\tilde{R}\left(\frac{\omega}{\epsilon}, \kappa_z; L - \eta\right)$, the characterization of $P(\vec{x}, t)$ requires the moments of the transmission and reflection coefficients. In this paper, we need just a few facts about these moments, which we quote from [1, 18, 16, 20]:

(1) The reflection coefficient $\tilde{R}\left(\frac{\omega}{\epsilon}, \kappa_z; L - \eta\right)$ is decorrelated from the transmission and reflection coefficients $T\left(\frac{\omega}{\epsilon}, \kappa_z; \eta\right)$ and $R\left(\frac{\omega}{\epsilon}, \kappa_z; \eta\right)$, as $\epsilon \rightarrow 0$. This is because they describe the behavior of the waves in two different parts of the random medium: in the bottom part $z \in (-L, -\eta)$ and the top part $z \in (-\eta, 0)$, respectively.

(2) For arbitrary frequencies ω, ω' and slowness vectors κ', κ' , we have, as $\epsilon \rightarrow 0$,

$$(3.8) \quad E \left\{ \mathcal{T} \left(\frac{\omega}{\epsilon}, \kappa_z \right) \overline{\mathcal{R} \left(\frac{\omega'}{\epsilon}, \kappa_{z'} \right)} \right\} \rightarrow 0.$$

(3) The coefficients \mathcal{R} decorrelate rapidly for frequencies and vertical slownesses that are not within an ϵ neighborhood of each other. Explicitly, we have, as $\epsilon \rightarrow 0$,

$$(3.9) \quad E \left\{ \mathcal{R} \left(\frac{\omega}{\epsilon}, \kappa_z \right) \overline{\mathcal{R} \left(\frac{\omega'}{\epsilon}, \kappa_{z'} \right)} \right\} \rightarrow 0,$$

when $|\omega - \omega'| > O(\epsilon)$ and/or $|\kappa_z - \kappa_{z'}| > O(\epsilon)$.

(4) The coefficients \mathcal{T} remain correlated, even for frequencies and slownesses that are more than ϵ apart. In fact, if either $|\omega - \omega'| > O(\epsilon)$ or $|\kappa_z - \kappa_{z'}| > O(\epsilon)$, we have

$$(3.10) \quad E \left\{ \mathcal{T} \left(\frac{\omega}{\epsilon}, \kappa_z \right) \overline{\mathcal{T} \left(\frac{\omega'}{\epsilon}, \kappa_{z'} \right)} \right\} \rightarrow E \left\{ K_{\text{ODA}}(\omega, \kappa_z; \eta) \overline{K_{\text{ODA}}(\omega', \kappa_{z'}; \eta)} \right\},$$

where K_{ODA} is the ODA kernel [24, 12, 5, 31]

$$(3.11) \quad K_{\text{ODA}}(\omega, \kappa_z; \eta) = \exp \left[\frac{i\omega W(\eta)}{c_o^2 \kappa_z} \sqrt{\frac{\ell}{2} - \frac{\omega^2 \ell \eta}{4c_o^4 \kappa_z^2}} \right],$$

and $W(\eta)$ is standard Brownian motion.

3.2. Imaging with the ODA kernel. The expression (2.20) of the coherent interferometric imaging functional and the forward model (3.6) show that $\mathcal{I}^{\text{CINT}}(\vec{\mathbf{y}}^s, \Omega_d)$ involves integrals over frequencies $\bar{\omega} \in [\omega_o - B, \omega_o + B]$, $\tilde{\omega} \in [-\Omega_d, \Omega_d]$ and over slownesses κ, κ' of the products $\mathcal{T}\left(\frac{\bar{\omega} + \tilde{\omega}/2}{\epsilon}, \kappa_z\right) \overline{\mathcal{T}\left(\frac{\bar{\omega} - \tilde{\omega}/2}{\epsilon}, \kappa_{z'}\right)}$, $\mathcal{T}\left(\frac{\bar{\omega} + \tilde{\omega}/2}{\epsilon}, \kappa_z\right) \overline{\mathcal{R}\left(\frac{\bar{\omega} - \tilde{\omega}/2}{\epsilon}, \kappa_{z'}\right)}$, and $\mathcal{R}\left(\frac{\bar{\omega} + \tilde{\omega}/2}{\epsilon}, \kappa_z\right) \overline{\mathcal{R}\left(\frac{\bar{\omega} - \tilde{\omega}/2}{\epsilon}, \kappa_{z'}\right)}$.

Now consider the expectation of $\mathcal{I}^{\text{CINT}}(\vec{\mathbf{y}}^s, \Omega_d)$ and use the asymptotic results of section 3.1. Because of the decorrelation of the reflection coefficients at different vertical slownesses and because of the integrals over κ and κ' , we see that, as $\epsilon \rightarrow 0$,

$$(3.12) \quad E \left\{ \mathcal{I}^{\text{CINT}}(\vec{\mathbf{y}}^s, \Omega_d) \right\} \rightarrow E \left\{ \mathcal{I}_{\text{ODA}}^{\text{CINT}}(\vec{\mathbf{y}}^s, \Omega_d) \right\},$$

where

(3.13)

$$\begin{aligned} \mathcal{I}_{\text{ODA}}^{\text{CINT}}(\vec{\mathbf{y}}^s, \Omega_d) &= \sum_{r=1}^N \sum_{r'=1}^N \int_{|\bar{\omega}-\omega_o| \leq B} \frac{d\bar{\omega}}{\epsilon} \int_{|\tilde{\omega}| \leq \Omega_d} \frac{d\tilde{\omega}}{\epsilon} \frac{(\bar{\omega}^2 - \frac{\tilde{\omega}^2}{4})^2}{\epsilon^4} \widehat{f}_B \left(\bar{\omega} + \frac{\tilde{\omega}}{2} - \omega_o \right) \\ &\quad \times \overline{\widehat{f}_B \left(\bar{\omega} - \frac{\tilde{\omega}}{2} - \omega_o \right)} \int d\boldsymbol{\kappa} \int d\boldsymbol{\kappa}' K_{\text{ODA}} \left(\bar{\omega} + \frac{\tilde{\omega}}{2}, \kappa_z \right) \overline{K_{\text{ODA}} \left(\bar{\omega} - \frac{\tilde{\omega}}{2}, \kappa_z' \right)} \\ &\quad \times \exp \left\{ i \frac{\bar{\omega} + \frac{\tilde{\omega}}{2}}{\epsilon} [(\boldsymbol{\kappa}, \kappa_z) \cdot (\vec{\mathbf{x}}_r - \vec{\mathbf{y}}) - \tau(\vec{\mathbf{x}}_r, \vec{\mathbf{y}}^s)] \right. \\ &\quad \left. - i \frac{\bar{\omega} - \frac{\tilde{\omega}}{2}}{\epsilon} [(\boldsymbol{\kappa}', \kappa_z') \cdot (\vec{\mathbf{x}}_{r'} - \vec{\mathbf{y}}) - \tau(\vec{\mathbf{x}}_{r'}, \vec{\mathbf{y}}^s)] \right\}. \end{aligned}$$

In fact, all the moments of $\mathcal{I}^{\text{CINT}}(\vec{\mathbf{y}}^s, \Omega_d)$ and $\mathcal{I}_{\text{ODA}}^{\text{CINT}}(\vec{\mathbf{y}}^s, \Omega_d)$ are the same in the asymptotic limit $\epsilon \rightarrow 0$, and one can show (see, for example, [22]) that $\mathcal{I}^{\text{CINT}}(\vec{\mathbf{y}}^s, \Omega_d)$ converges in distribution to $\mathcal{I}_{\text{ODA}}^{\text{CINT}}(\vec{\mathbf{y}}^s, \Omega_d)$, the imaging function given by the ODA kernel.

A similar result can be obtained for Kirchhoff migration, so we conclude that in the asymptotic limit $\epsilon \rightarrow 0$, only the ODA kernel (i.e., the coherent part of the signal) matters in both Kirchhoff and coherent interferometric imaging. Naturally, ϵ will be small but finite in general, so this statement should be taken in an approximate sense. It is important to note that the asymptotic approximation of $\mathcal{I}^{\text{CINT}}$ by $\mathcal{I}_{\text{ODA}}^{\text{CINT}}$ is more robust than that of Kirchhoff migration because of the statistical smoothing introduced with the parameter Ω_d .

4. Resolution analysis. We have seen in section 3.2 that the coherent interferometric imaging function converges in distribution to $\mathcal{I}_{\text{ODA}}^{\text{CINT}}$, given by (3.13), so let us consider its resolution limits. We begin by describing in section 4.1 the data acquisition geometry and the time windowing of the traces. Then we obtain the resolution limits in section 4.2.

4.1. The array data and acquisition geometry. Recall that the surface of measurements is at $z = 0$, and let $\vec{\mathbf{x}} = (\mathbf{x}, 0)$ be an arbitrary location in the array. We simplify the notation with

$$(4.1) \quad \tau((\mathbf{x}, 0), \vec{\mathbf{y}}^s) \rightsquigarrow \tau(\mathbf{x}, \vec{\mathbf{y}}), \quad |(\mathbf{x}, 0) - \vec{\mathbf{y}}^s| = r(\mathbf{x}, \vec{\mathbf{y}}^s),$$

and suppose that we record the trace at $\vec{\mathbf{x}}$ over a time window $\psi(t)$ asymptotically independent of ϵ , centered at the deterministic arrival time

$$(4.2) \quad \tau(\mathbf{x}, \vec{\mathbf{y}}) = \frac{r(\mathbf{x}, \vec{\mathbf{y}})}{c}.$$

The measured pressure field is

$$(4.3) \quad P^\psi(t, \vec{\mathbf{x}}) = P(t, \vec{\mathbf{x}}) \psi(t - \tau(\mathbf{x}, \vec{\mathbf{y}}))$$

with Fourier coefficient

$$\begin{aligned}
\widehat{P}^\psi\left(\frac{\omega}{\epsilon}, \bar{\mathbf{x}}\right) &= \int dt P^\psi(t, \bar{\mathbf{x}}) e^{i\frac{\omega}{\epsilon}t} = \frac{1}{2\pi\epsilon} \int d\omega' \widehat{P}\left(\frac{\omega'}{\epsilon}, \bar{\mathbf{x}}\right) \widehat{\psi}\left(\frac{\omega - \omega'}{\epsilon}\right) e^{i\frac{(\omega - \omega')}{\epsilon}\tau(\mathbf{x}, \bar{\mathbf{y}})} \\
(4.4) \quad &= \frac{1}{2\pi} \int du \widehat{P}\left(\frac{\omega - \epsilon u}{\epsilon}, \bar{\mathbf{x}}\right) \widehat{\psi}(u) e^{iu\tau(\mathbf{x}, \bar{\mathbf{y}})},
\end{aligned}$$

where the domain of integration in u is determined by the bandwidth of the window, that is, $O(1)$.

In the following section we use the windowed pressure field (4.3) for imaging the source location $\bar{\mathbf{y}}$. This requires measurements at various locations $\bar{\mathbf{x}}$ in the array. Naturally, we can have many acquisition geometries, but under our assumption of small aperture $a \ll \eta$ the results come out essentially the same for most data gathering setups. Therefore, let us choose a common midpoint geometry, where we measure P^ψ at transducer locations $\bar{\mathbf{x}}_r = (\mathbf{x}_r, 0)$, $\bar{\mathbf{x}}'_r = (\mathbf{x}'_r, 0)$ satisfying

$$(4.5) \quad \bar{\mathbf{x}} = \frac{\mathbf{x}_r + \mathbf{x}'_r}{2}, \quad \tilde{\mathbf{x}}_r = \mathbf{x}_r - \mathbf{x}'_r,$$

for $\bar{\mathbf{x}} = \mathbf{x}_c$, the center of the array, and $\tilde{\mathbf{x}}_r$ varying with $r = 1, 2, \dots, N/2$.

The array aperture is small, when compared to the range η , so let us suppose that

$$(4.6) \quad a \text{ is proportional to } \delta, \quad \epsilon \ll \delta \ll 1, \quad \delta^2 \leq \epsilon,$$

where the latter condition allows us to linearize the deterministic phases in $\mathcal{I}_{\text{ODA}}^{\text{CINT}}$ and thus to simplify the calculations in section 4.2. Of course, one can take large apertures too, in which case the analysis of section 4.2 should be modified accordingly.

Finally, we note that in our resolution analysis, we suppose that Ω_d satisfies

$$(4.7) \quad \epsilon \ll \Omega_d = O(\gamma) \ll B,$$

with B independent of ϵ . Here the upper bound is needed for the statistical smoothing, and the lower bound says that there is enough coherence in the data to have some resolution.

4.2. Resolution study. The imaging function $\mathcal{I}_{\text{ODA}}^{\text{CINT}}(\bar{\mathbf{y}}^s; \bar{\mathbf{x}}, \Omega_d)$ is given by (recall (3.13))

$$\begin{aligned}
(4.8) \quad \mathcal{I}_{\text{ODA}}^{\text{CINT}}(\bar{\mathbf{y}}^s, \Omega_d; \bar{\mathbf{x}}) &\sim \sum_{r=1}^{N/2} \int_{|\bar{\omega} - \omega_0| \leq B} d\bar{\omega} \int_{|\bar{\omega}| \leq \Omega_d} d\bar{\omega} \\
&\times \widehat{P}_{\text{ODA}}^\psi\left(\frac{\bar{\omega} + \frac{\bar{\omega}}{2}}{\epsilon}, \bar{\mathbf{x}} + \frac{\tilde{\mathbf{x}}_r}{2}\right) \overline{\widehat{P}_{\text{ODA}}^\psi\left(\frac{\bar{\omega} - \frac{\bar{\omega}}{2}}{\epsilon}, \bar{\mathbf{x}} - \frac{\tilde{\mathbf{x}}_r}{2}\right)} \\
&\times \exp\left\{-i\left(\frac{\bar{\omega} + \frac{\bar{\omega}}{2}}{\epsilon}\right)\tau\left(\bar{\mathbf{x}} + \frac{\tilde{\mathbf{x}}_r}{2}, \bar{\mathbf{y}}^s\right) + i\left(\frac{\bar{\omega} - \frac{\bar{\omega}}{2}}{\epsilon}\right)\tau\left(\bar{\mathbf{x}} - \frac{\tilde{\mathbf{x}}_r}{2}, \bar{\mathbf{y}}^s\right)\right\},
\end{aligned}$$

where

$$\begin{aligned}
(4.9) \quad \widehat{P}_{\text{ODA}}^\psi\left(\frac{\omega}{\epsilon}, \vec{\mathbf{x}}\right) &= \frac{1}{16\pi^3} \int du \widehat{\psi}(u) \left(\frac{\omega - \epsilon u}{\epsilon}\right)^2 \widehat{f}_B(\omega - \omega_0 - \epsilon u) \int d\boldsymbol{\kappa} K_{\text{ODA}}(\omega - \epsilon u, \boldsymbol{\kappa}_z) \\
&\quad \times e^{i\left(\frac{\omega}{\epsilon} - u\right)(\boldsymbol{\kappa}, \boldsymbol{\kappa}_z) \cdot (\mathbf{x} - \boldsymbol{\xi}, \eta) + iu\tau(\mathbf{x}, \vec{\mathbf{y}})} \\
&\approx \frac{\omega^2 \widehat{f}_B(\omega - \omega_0)}{16\pi^2 \epsilon^2} \int du \widehat{\chi}(u) \int d\boldsymbol{\kappa} K_{\text{ODA}}(\omega, \boldsymbol{\kappa}_z) e^{i\left(\frac{\omega}{\epsilon} - u\right)(\boldsymbol{\kappa}, \boldsymbol{\kappa}_z) \cdot (\mathbf{x} - \boldsymbol{\xi}, \eta) + iu\tau(\mathbf{x}, \vec{\mathbf{y}})},
\end{aligned}$$

and where the integral over $\boldsymbol{\kappa}$ can be approximated with the method of stationary phase. The rapid phase is

$$(4.10) \quad \phi(\boldsymbol{\kappa}) = \frac{\omega}{\epsilon} (\boldsymbol{\kappa}, \boldsymbol{\kappa}_z) \cdot (\mathbf{x} - \boldsymbol{\xi}, \eta), \quad \text{where } \boldsymbol{\kappa}_z = \frac{\sqrt{1 - c_o^2 \boldsymbol{\kappa}^2}}{c_o},$$

so the main contribution to the $\boldsymbol{\kappa}$ integral comes from slowness vectors $\boldsymbol{\kappa}^*$ satisfying $\nabla\phi(\boldsymbol{\kappa}^*) = \mathbf{0}$. We easily find that

$$(4.11) \quad \boldsymbol{\kappa}^* = \frac{\mathbf{x} - \boldsymbol{\xi}}{c_o r(\mathbf{x}, \vec{\mathbf{y}})}$$

and the stationary phase approximation of (4.9) is

$$\begin{aligned}
(4.12) \quad \widehat{P}_{\text{ODA}}^\psi\left(\frac{\omega}{\epsilon}, \vec{\mathbf{x}}\right) &\approx \frac{\omega \widehat{f}_B(\omega - \omega_0) \eta}{8\pi \epsilon c_o^3 \tau^2(\mathbf{x}, \vec{\mathbf{y}})} K_{\text{ODA}}(\omega, \boldsymbol{\kappa}_z^*) \exp\left\{i\frac{\omega}{\epsilon} \tau(\mathbf{x}, \vec{\mathbf{y}})\right\} \int du \widehat{\psi}(u) \\
&= \frac{\omega \widehat{f}_B(\omega - \omega_0) \sin^2 \theta(\mathbf{x})}{8\pi \epsilon c_o \eta} \exp\left\{i\frac{\omega}{\epsilon} \tau(\mathbf{x}, \vec{\mathbf{y}}) + i\omega \frac{T_{\text{ps}}}{\sin \theta(\mathbf{x})} \frac{W(\eta)}{\sqrt{\eta}} - \frac{\omega^2 T_{\text{ps}}^2}{2 \sin^2 \theta(\mathbf{x})}\right\},
\end{aligned}$$

where we set

$$(4.13) \quad \int du \widehat{\psi}(u) = \psi(0) = 1$$

and define $\sin \theta(\mathbf{x}) = \eta / r(\mathbf{x}, \vec{\mathbf{y}})$ and the pulse spread time parameter

$$(4.14) \quad T_{\text{ps}} = \frac{1}{c_o} \sqrt{\frac{\ell \eta}{2}}.$$

The imaging function becomes, after approximating $\widehat{f}_B(\bar{\omega} \pm \frac{\bar{\omega}}{2} - \omega_0) \approx f_B(\bar{\omega} - \omega_0)$

and setting $\tau(\bar{\mathbf{x}} \pm \tilde{\mathbf{x}}_r/2, \bar{\mathbf{y}}) \approx \tau(\bar{\mathbf{x}}, \bar{\mathbf{y}})$ in the amplitude,

(4.15)

$$\begin{aligned} \mathcal{I}_{\text{ODA}}^{\text{CINT}}(\bar{\mathbf{y}}^s, \Omega_d; \bar{\mathbf{x}}) &\sim \sum_{r=1}^{N/2} \frac{\eta^2}{\tau^4(\bar{\mathbf{x}}, \bar{\mathbf{y}})} \int_{|\bar{\omega}-\omega_0| \leq B} d\bar{\omega} \bar{\omega}^2 |\hat{f}_B(\bar{\omega} - \omega_0)|^2 \int_{|\bar{\omega}| \leq \Omega_d} d\tilde{\omega} \\ &\quad \times e^{i\left(\frac{\bar{\omega} + \frac{\tilde{\omega}}{\epsilon}}{\epsilon}\right) [\tau(\bar{\mathbf{x}} + \frac{\tilde{\mathbf{x}}_r}{2}, \bar{\mathbf{y}}) - \tau(\bar{\mathbf{x}} + \frac{\tilde{\mathbf{x}}_r}{2}, \bar{\mathbf{y}}^s)] - i\left(\frac{\bar{\omega} - \frac{\tilde{\omega}}{\epsilon}}{\epsilon}\right) [\tau(\bar{\mathbf{x}} - \frac{\tilde{\mathbf{x}}_r}{2}, \bar{\mathbf{y}}) - \tau(\bar{\mathbf{x}} - \frac{\tilde{\mathbf{x}}_r}{2}, \bar{\mathbf{y}}^s)]} \\ &\quad \times e^{i\bar{\omega} T_{\text{ps}} \frac{W(\eta)}{\sqrt{\eta}} [\sin^{-1} \theta(\bar{\mathbf{x}} + \frac{\tilde{\mathbf{x}}_r}{2}) - \sin^{-1} \theta(\bar{\mathbf{x}} - \frac{\tilde{\mathbf{x}}_r}{2})] + i\tilde{\omega} T_{\text{ps}} \frac{W(\eta)}{\sqrt{\eta}} \frac{1}{2} [\sin^{-1} \theta(\bar{\mathbf{x}} + \frac{\tilde{\mathbf{x}}_r}{2}) + \sin^{-1} \theta(\bar{\mathbf{x}} - \frac{\tilde{\mathbf{x}}_r}{2})]} \\ &\quad \times e^{-\bar{\omega}^2 T_{\text{ps}}^2 \frac{1}{2} [\sin^{-2} \theta(\bar{\mathbf{x}} + \frac{\tilde{\mathbf{x}}_r}{2}) + \sin^{-2} \theta(\bar{\mathbf{x}} - \frac{\tilde{\mathbf{x}}_r}{2})] - \frac{\tilde{\omega}^2}{8} T_{\text{ps}}^2 [\sin^{-2} \theta(\bar{\mathbf{x}} + \frac{\tilde{\mathbf{x}}_r}{2}) + \sin^{-2} \theta(\bar{\mathbf{x}} - \frac{\tilde{\mathbf{x}}_r}{2})]} \\ &\quad \times e^{-\bar{\omega} \tilde{\omega} T_{\text{ps}}^2 [\sin^{-2} \theta(\bar{\mathbf{x}} + \frac{\tilde{\mathbf{x}}_r}{2}) - \sin^{-2} \theta(\bar{\mathbf{x}} - \frac{\tilde{\mathbf{x}}_r}{2})]}. \end{aligned}$$

Now let us recall that the array aperture is small and linearize the phases in (4.15) as

$$(4.16) \quad \begin{aligned} \tau\left(\bar{\mathbf{x}} + \frac{\tilde{\mathbf{x}}_r}{2}, \bar{\mathbf{y}}\right) - \tau\left(\bar{\mathbf{x}} - \frac{\tilde{\mathbf{x}}_r}{2}, \bar{\mathbf{y}}\right) &\approx \tilde{\mathbf{x}}_r \cdot \nabla_{\bar{\mathbf{x}}} \tau(\bar{\mathbf{x}}, \bar{\mathbf{y}}), \\ \frac{1}{2} \left[\tau\left(\bar{\mathbf{x}} + \frac{\tilde{\mathbf{x}}_r}{2}, \bar{\mathbf{y}}\right) + \tau\left(\bar{\mathbf{x}} - \frac{\tilde{\mathbf{x}}_r}{2}, \bar{\mathbf{y}}\right) \right] &\approx \tau(\bar{\mathbf{x}}, \bar{\mathbf{y}}). \end{aligned}$$

We also have

(4.17)

$$\begin{aligned} \sin^{-1} \theta\left(\bar{\mathbf{x}} + \frac{\tilde{\mathbf{x}}_r}{2}\right) - \sin^{-1} \theta\left(\bar{\mathbf{x}} - \frac{\tilde{\mathbf{x}}_r}{2}\right) &\approx \tilde{\mathbf{x}}_r \cdot \nabla_{\bar{\mathbf{x}}} \sin^{-1} \theta(\bar{\mathbf{x}}) = -\tilde{\mathbf{x}}_r \cdot \frac{(\bar{\mathbf{x}} - \boldsymbol{\xi})}{\eta r(\bar{\mathbf{x}}, \bar{\mathbf{y}})}, \\ \frac{1}{2} \left[\sin^{-1} \theta\left(\bar{\mathbf{x}} + \frac{\tilde{\mathbf{x}}_r}{2}\right) + \sin^{-1} \theta\left(\bar{\mathbf{x}} - \frac{\tilde{\mathbf{x}}_r}{2}\right) \right] &\approx \sin^{-1} \theta(\bar{\mathbf{x}}) = \frac{r(\bar{\mathbf{x}}, \bar{\mathbf{y}})}{\eta}, \\ \frac{1}{2} \left[\sin^{-2} \theta\left(\bar{\mathbf{x}} + \frac{\tilde{\mathbf{x}}_r}{2}\right) + \sin^{-2} \theta\left(\bar{\mathbf{x}} - \frac{\tilde{\mathbf{x}}_r}{2}\right) \right] &\approx \sin^{-2} \theta(\bar{\mathbf{x}}) = \left(\frac{r(\bar{\mathbf{x}}, \bar{\mathbf{y}})}{\eta}\right)^2, \end{aligned}$$

so neglecting quadratic terms of $O(\gamma\delta + \gamma^2)$ (recall (4.6)–(4.7)) and approximating the sum over the array by an integral over the aperture, we have

(4.18)

$$\begin{aligned} \mathcal{I}_{\text{ODA}}^{\text{CINT}}(\bar{\mathbf{y}}^s, \Omega_d; \bar{\mathbf{x}}) &\sim \frac{\eta^2}{\tau^4(\bar{\mathbf{x}}, \bar{\mathbf{y}})} \int_{|\bar{\mathbf{x}}| \leq a} d\tilde{\mathbf{x}} \int_{|\bar{\omega}-\omega_0| \leq B} d\bar{\omega} \frac{\bar{\omega}^2 |\hat{f}_B(\bar{\omega} - \omega_0)|^2}{\epsilon^2} e^{-\frac{\bar{\omega}^2 T_{\text{ps}}^2}{\sin^2 \theta(\bar{\mathbf{x}})}} \\ &\quad \times e^{i\frac{\tilde{\omega}}{\epsilon} \tilde{\mathbf{x}} \cdot [\nabla_{\bar{\mathbf{x}}} \tau(\bar{\mathbf{x}}, \bar{\mathbf{y}}) - \nabla_{\bar{\mathbf{x}}} \tau(\bar{\mathbf{x}}, \bar{\mathbf{y}}^s)] + \epsilon T_{\text{ps}} \sin \theta(\bar{\mathbf{x}}) \frac{\bar{\mathbf{x}} - \boldsymbol{\xi}}{\eta^2} \frac{W(\eta)}{\sqrt{\eta}}} \\ &\quad \times \int_{|\bar{\omega}| \leq \Omega_d} d\tilde{\omega} e^{i\frac{\tilde{\omega}}{\epsilon} [\tau(\bar{\mathbf{x}}, \bar{\mathbf{y}}) - \tau(\bar{\mathbf{x}}, \bar{\mathbf{y}}^s) + \frac{\epsilon T_{\text{ps}}}{\sin \theta(\bar{\mathbf{x}})} \frac{W(\eta)}{\sqrt{\eta}}]}. \end{aligned}$$

The evaluation of $\mathcal{I}_{\text{ODA}}^{\text{CINT}}$ is now reduced to the computation of the integrals in $\tilde{\omega}$,

$\tilde{\mathbf{x}}$, and $\bar{\omega}$. The integral over $\tilde{\omega}$ is

$$(4.19) \quad \begin{aligned} \mathcal{F}_{\tilde{\omega}} &= \int_{|\tilde{\omega}| \leq \Omega_d} d\tilde{\omega} e^{i\frac{\tilde{\omega}}{\epsilon} \left[\tau(\bar{\mathbf{x}}, \bar{\mathbf{y}}) - \tau(\bar{\mathbf{x}}, \bar{\mathbf{y}}^s) + \frac{\epsilon T_{\text{ps}}}{\sin \theta(\bar{\mathbf{x}})} \frac{W(\eta)}{\sqrt{\eta}} \right]} \\ &\approx 2 \frac{\sin \left\{ \frac{\Omega_d}{\epsilon} \left[\tau(\bar{\mathbf{x}}, \bar{\mathbf{y}}) - \tau(\bar{\mathbf{x}}, \bar{\mathbf{y}}^s) + \frac{\epsilon T_{\text{ps}}}{\sin \theta(\bar{\mathbf{x}})} \frac{W(\eta)}{\sqrt{\eta}} \right] \right\}}{\left[\tau(\bar{\mathbf{x}}, \bar{\mathbf{y}}) - \tau(\bar{\mathbf{x}}, \bar{\mathbf{y}}^s) + \frac{\epsilon T_{\text{ps}}}{\sin \theta(\bar{\mathbf{x}})} \frac{W(\eta)}{\sqrt{\eta}} \right]} \end{aligned}$$

and the integral over $\tilde{\mathbf{x}}$ gives

$$(4.20) \quad \mathcal{F}_{\tilde{\mathbf{x}}} = \int_{|\tilde{\mathbf{x}}| \leq a} d\tilde{\mathbf{x}} e^{i\frac{\tilde{\omega}}{\epsilon} \tilde{\mathbf{x}} \cdot \left[\nabla_{\bar{\mathbf{x}}} \tau(\bar{\mathbf{x}}, \bar{\mathbf{y}}) - \nabla_{\bar{\mathbf{x}}} \tau(\bar{\mathbf{x}}, \bar{\mathbf{y}}^s) + \epsilon T_{\text{ps}} \sin \theta(\bar{\mathbf{x}}) \frac{\bar{\mathbf{x}} - \boldsymbol{\xi}}{\eta^2} \frac{W(\eta)}{\sqrt{\eta}} \right]} = 4 \frac{\sin\left(\frac{a\tilde{\omega}\phi_1}{\epsilon}\right) \sin\left(\frac{a\tilde{\omega}\phi_2}{\epsilon}\right)}{\frac{\tilde{\omega}}{\epsilon}\phi_1 \frac{\tilde{\omega}}{\epsilon}\phi_2},$$

where

$$(4.21) \quad \begin{aligned} \phi_1 &= \bar{\mathbf{e}}_1 \cdot \left[\nabla_{\bar{\mathbf{x}}} \tau(\bar{\mathbf{x}}, \bar{\mathbf{y}}) - \nabla_{\bar{\mathbf{x}}} \tau(\bar{\mathbf{x}}, \bar{\mathbf{y}}^s) + \epsilon T_{\text{ps}} \sin \theta(\bar{\mathbf{x}}) \frac{\bar{\mathbf{x}} - \boldsymbol{\xi}}{\eta^2} \frac{W(\eta)}{\sqrt{\eta}} \right], \\ \phi_2 &= \bar{\mathbf{e}}_2 \cdot \left[\nabla_{\bar{\mathbf{x}}} \tau(\bar{\mathbf{x}}, \bar{\mathbf{y}}) - \nabla_{\bar{\mathbf{x}}} \tau(\bar{\mathbf{x}}, \bar{\mathbf{y}}^s) + \epsilon T_{\text{ps}} \sin \theta(\bar{\mathbf{x}}) \frac{\bar{\mathbf{x}} - \boldsymbol{\xi}}{\eta^2} \frac{W(\eta)}{\sqrt{\eta}} \right]. \end{aligned}$$

Finally, to compute the integral over $\bar{\omega}$,

$$(4.22) \quad \mathcal{F}_{\bar{\omega}} = \int_{|\bar{\omega} - \omega_o| \leq B} d\bar{\omega} |\hat{f}_B(\bar{\omega} - \omega_o)|^2 e^{-\frac{\bar{\omega}^2 T_{\text{ps}}^2}{\sin^2 \theta(\bar{\mathbf{x}})}} \left\{ \cos \left[\frac{a\bar{\omega}(\phi_1 - \phi_2)}{\epsilon} \right] - \cos \left[\frac{a\bar{\omega}(\phi_1 + \phi_2)}{\epsilon} \right] \right\},$$

we suppose that we have the Gaussian pulse

$$(4.23) \quad \hat{f}_B(\bar{\omega} - \omega_o) = e^{-\frac{T_p^2(\bar{\omega} - \omega_o)^2}{2}},$$

with support $O(1/T_p) \sim B$. The integral (4.22) is

$$(4.24) \quad \begin{aligned} \mathcal{F}_{\bar{\omega}} &\sim \frac{1}{\phi_1 \phi_2} e^{-\frac{a^2(\phi_1^2 + \phi_2^2)}{4\epsilon^2 \left(T_p^2 + \frac{T_{\text{ps}}^2}{\sin^2 \theta(\bar{\mathbf{x}})} \right)}} \\ &\times \left\{ \sin \left[\frac{a\omega_o \phi_1}{\epsilon \left(1 + \frac{T_{\text{ps}}^2}{T_p^2 \sin^2 \theta(\bar{\mathbf{x}})} \right)} \right] \sin \left[\frac{a\omega_o \phi_2}{\epsilon \left(1 + \frac{T_{\text{ps}}^2}{T_p^2 \sin^2 \theta(\bar{\mathbf{x}})} \right)} \right] \cosh \left[\frac{\phi_1 \phi_2 a^2}{2\epsilon^2 \left(T_p^2 + \frac{T_{\text{ps}}^2}{\sin^2 \theta(\bar{\mathbf{x}})} \right)} \right] \right. \\ &\left. + \cos \left[\frac{a\omega_o \phi_1}{\epsilon \left(1 + \frac{T_{\text{ps}}^2}{T_p^2 \sin^2 \theta(\bar{\mathbf{x}})} \right)} \right] \cos \left[\frac{a\omega_o \phi_2}{\epsilon \left(1 + \frac{T_{\text{ps}}^2}{T_p^2 \sin^2 \theta(\bar{\mathbf{x}})} \right)} \right] \sinh \left[\frac{\phi_1 \phi_2 a^2}{2\epsilon^2 \left(T_p^2 + \frac{T_{\text{ps}}^2}{\sin^2 \theta(\bar{\mathbf{x}})} \right)} \right] \right\}, \end{aligned}$$

and it is a highly peaked function near the origin $\phi_1 = \phi_2 = 0$, as one can see by plotting it.

Because formula (4.24) is rather complicated, to get an idea about the resolution limit, let us look along the line $\phi_2 = 0$ in the two-dimensional plane. Then (4.24) becomes

$$(4.25) \quad \mathcal{F}_{\bar{\omega}}|_{\phi_2=0} \sim \frac{\sin \left[\frac{a\omega_o \phi_1}{\epsilon \left(1 + \frac{T_{ps}^2}{T_p^2 \sin^2 \theta(\bar{\mathbf{x}})} \right)} \right]}{\phi_1} e^{-\frac{a^2 \phi_1^2}{4\epsilon^2 \left(T_p^2 + \frac{T_{ps}^2}{\sin^2 \theta(\bar{\mathbf{x}})} \right)}},$$

so the uncertainty in ϕ_1 is determined by

$$(4.26) \quad \frac{\epsilon}{aB_{ps}} = \min \left\{ \frac{\epsilon}{aB} \sqrt{1 + \frac{T_{ps}^2}{T_p^2 \sin^2 \theta(\bar{\mathbf{x}})}}, \frac{\epsilon}{a\omega_o} \left(1 + \frac{T_{ps}^2}{T_p^2 \sin^2 \theta(\bar{\mathbf{x}})} \right) \right\},$$

where we used that $1/T_p \sim B$. Obviously, the same conclusion holds for the uncertainty of ϕ_2 if we set $\phi_1 = 0$. Thus, gathering all our results and neglecting the $O(\epsilon)$ random shifts in (4.19) and (4.21), we have the resolution limits

$$(4.27) \quad r(\bar{\mathbf{x}}, \bar{\mathbf{y}}) - r(\bar{\mathbf{x}}, \bar{\mathbf{y}}^s) \leq O\left(\frac{\epsilon \pi c_o}{\Omega_d}\right), \quad \left| \frac{\bar{\mathbf{x}} - \boldsymbol{\xi}}{r(\bar{\mathbf{x}}, \bar{\mathbf{y}})} - \frac{\bar{\mathbf{x}} - \boldsymbol{\xi}^s}{r(\bar{\mathbf{x}}, \bar{\mathbf{y}}^s)} \right| \leq O\left(\frac{\epsilon \pi c_o}{B_{ps} a}\right).$$

5. Summary. We have shown that, as in [10] for isotropic random media, the coherent interferometric functional (2.18), which can be considered to be a smoothed version of the square of the Kirchhoff migration functional (1.3), gives statistically stable images in cluttered media that are finely layered. When the smoothing parameter Ω_d , which is also the decoherence frequency of the array data, is chosen adaptively and in a suitably defined optimal way (see Remark 1 in section 2.5), then there is minimal loss of resolution and the images are stable. The properties of the coherent interferometric functional (2.18) are first discussed informally in a physical way, as in [10] for the isotropic case, and then analyzed from first principles using the extensive theory of waves in randomly layered media. The main result is that, as in [10], the range resolution is proportional to c_0/Ω_d . Since the decoherence frequency is usually much smaller than the bandwidth, this result expresses in a clear and effective manner the loss of range resolution due to the random layering. Contrary to what happens in isotropic random media, analyzed in [10], there is no loss of cross-range resolution in randomly layered media. We illustrate in section 2.5 with numerical simulations the effectiveness of coherent interferometry for imaging in finely layered random media.

REFERENCES

- [1] M. ASCH, W. KÖHLER, G. PAPANICOLAOU, M. POSTEL, AND B. WHITE, *Frequency content of randomly scattered signals*, SIAM Rev., 33 (1991), pp. 519–625.
- [2] E. BÉCACHE, P. JOLY, AND C. TSOGKA, *Etude d'un nouvel élément fini mixte permettant la condensation de masse*, C. R. Acad. Sci. Paris Sér. I Math., 324 (1997), pp. 1281–1286.
- [3] E. BÉCACHE, P. JOLY, AND C. TSOGKA, *An analysis of new mixed finite elements for the approximation of wave propagation problems*, SIAM J. Numer. Anal., 37 (2000), pp. 1053–1084.
- [4] J. P. BÉRENGER, *A perfectly matched layer for the absorption of electromagnetic waves*, J. Comput. Phys., 114 (1994), pp. 185–200.
- [5] L. BERLYAND AND R. BURRIDGE, *The accuracy of the O'Doherty-Anstey approximation for waves propagating in highly disordered stratified media*, Wave Motion, 21 (1995), pp. 357–373.
- [6] G. BEYLKIN, *Imaging of discontinuities in the inverse scattering problem by inversion of a causal generalized Radon transform*, J. Math. Phys., 26 (1985), pp. 99–108.

- [7] N. BLEISTEIN, J. K. COHEN, AND J. W. STOCKWELL, JR., *Mathematics of Multidimensional Seismic Imaging, Migration, and Inversion*, Springer, New York, 2001.
- [8] L. BORCEA, G. PAPANICOLAOU, AND C. TSOGKA, *Theory and applications of time reversal and interferometric imaging*, *Inverse Problems*, 19 (2003), pp. S139–S164.
- [9] L. BORCEA, G. PAPANICOLAOU, AND C. TSOGKA, *Adaptive interferometric imaging in clutter*, *Inverse Problems*, submitted.
- [10] L. BORCEA, G. PAPANICOLAOU, AND C. TSOGKA, *Interferometric array imaging in clutter*, *Inverse Problems*, 21 (2005), pp. 1419–1460.
- [11] B. BORDEN, *Mathematical problems in radar inverse scattering*, *Inverse Problems*, 19 (2002), pp. R1–R28.
- [12] R. BURRIDGE, G. PAPANICOLAOU, P. SHENG, AND B. WHITE, *Probing a random medium with a pulse*, *SIAM J. Appl. Math.*, 49 (1989), pp. 582–607.
- [13] R. BURRIDGE, G. PAPANICOLAOU, AND B. WHITE, *Statistics for pulse reflection from a randomly layered medium*, *SIAM J. Appl. Math.*, 47 (1987), pp. 146–168.
- [14] T. K. CHAN, Y. KUGA, AND A. ISHIMARU, *Experimental studies on circular sar imaging in clutter using angular correlation function technique*, *IEEE Trans. Geosci. Remote Sensing*, 37 (1999), pp. 2192–2197.
- [15] M. CHENEY, *A mathematical tutorial on synthetic aperture radar*, *SIAM Rev.*, 43 (2001), pp. 301–312.
- [16] J. CHILLAN AND J. P. FOUQUE, *Pressure fields generated by acoustical pulses propagating in randomly layered media*, *SIAM J. Appl. Math.*, 58 (1998), pp. 1532–1546.
- [17] J. F. CLAERBOUT, *Fundamentals of Geophysical Data Processing: With Applications to Petroleum Prospecting*, Blackwell Scientific Publications, Palo Alto, CA, 1985.
- [18] J. F. CLOUET AND J. P. FOUQUE, *Spreading of a pulse travelling in random media*, *Ann. Appl. Probab.*, 4 (1994), pp. 1083–1097.
- [19] J. C. CURLANDER AND R. N. MCDONOUGH, *Synthetic Aperture Radar*, Wiley, New York, 1991.
- [20] J. P. FOUQUE, S. GARNIER, A. NACHBIN, AND K. SØLNA, *Time-reversal refocusing for point source in randomly layered media*, *Wave Motion*, 42 (2005), pp. 238–260.
- [21] J. P. FOUQUE AND K. SOLNA, *Time-reversal aperture enhancement*, *Multiscale Model. Simul.*, 1 (2003), pp. 239–259.
- [22] J. GARNIER, *Imaging in randomly layered media by cross-correlating noisy signals*, *Multiscale Model. Simul.*, 4 (2005), pp. 610–640.
- [23] H. KESTEN AND G. PAPANICOLAOU, *A limit theorem for turbulent diffusion*, *Comm. Math. Phys.*, 65 (1979), pp. 97–128.
- [24] R. F. O'DOHERTY AND N. A. ANSTEY, *Reflections on amplitudes*, *Geophys. Prospecting*, 19 (1971), pp. 430–458.
- [25] G. PAPANICOLAOU, M. POSTEL, P. SHENG, AND B. WHITE, *Frequency content of randomly scattered signals II: Inversion*, *Wave Motion*, 12 (1990), pp. 527–549.
- [26] G. C. PAPANICOLAOU, D. STROOCK, AND S. R. S. VARADHAN, *Martingale approach to some limit theorems*, in *Statistical Mechanics, Dynamical Systems and the Duke Turbulence Conference*, Duke Univ. Math. Ser. 3, D. Ruelle, ed., Duke University, Durham, NC, 1977.
- [27] G. C. PAPANICOLAOU AND S. R. S. VARADHAN, *A limit theorem with strong mixing in Banach space and two applications to stochastic differential equations*, *Comm. Pure Appl. Math.*, 26 (1973), pp. 497–524.
- [28] M. B. PRIESTLEY, *Spectral Analysis and Time Series*, Academic Press, London, New York, 1981.
- [29] L. I. RUDIN, S. OSHER, AND E. FATEMI, *Nonlinear total variation based noise removal algorithms*, *Phys. D*, 60 (1992), pp. 259–268.
- [30] C. E. SHANNON AND W. WEAVER, *The Mathematical Theory of Communication*, University of Illinois Press, Champaign, IL, 1963.
- [31] K. SOLNA AND G. PAPANICOLAOU, *Ray theory for a locally layered random medium*, *Waves Random Media*, 10 (2000), pp. 151–198.